Mohedano, M.; Luthringer, B.J.C.; Mingo, B.; Feyerabend, F.; Arrabal, R.; Sanchez-Egido, P.J.; Blawert, C.; Willumeit-Roemer, R.; Zheludkevich, M.L.; Matykina, E.:

# Bioactive plasma electrolytic oxidation coatings on Mg-Ca alloy to control degradation behaviour

In: Surface and Coatings Technology (2017) Elsevier

DOI: 10.1016/j.surfcoat.2017.02.050

# Bioactive plasma electrolytic oxidation coatings on Mg-Ca alloy to control degradation behaviour

M. Mohedano[a,c], B.J.C. Luthringer[b], B. Mingo[c], F. Feyerabend[b], R. Arrabal[c], P. J. Sanchez-Egido[c], C. Blawert[a], R. Willumeit-Römer[b], M.L.Zheludkevich[a,d], E. Matykina[c]

[a]Institute of Materials Research, Helmholtz-ZentrumGeesthacht, Max-Planck-Straβe 1, 21502 Geesthacht, Germany

[b]Institute of Materials Research, Division of Metallic Biomaterials, Helmholtz-ZentrumGeesthacht, 21502 Geesthacht, Germany

[c]Departamento de Ciencia de Materiales, Facultad de Ciencias Químicas, Universidad Complutense, 28040 Madrid, Spain

[d]Department of Materials and Ceramic Engineering, CICECO – Aveiro Institute of Materials, University of Aveiro, 3810-193 Aveiro, Portugal

## Abstract

The present work reports on PEO coatings which can be potentially used for degradation control of Mg-based implant materials. Three coatings were developed on Mg-0.8wt%Ca alloy: two in an electrolyte with fluoride species using different treatment times and one in a fluoride-free electrolyte. Uncoated and coated materials were examined in terms of structure and morphology using TEM, SEM and XRD. The corrosion investigations on fluoride-containing samples were performed using DC potentiodynamic curves, EIS and hydrogen evolution measurements. Both PEO coatings improved the corrosion resistance compared to the bulk material and the best behaviour was found for the thinnest PEO coating (PEO1-F). The amount of released $F^-$ ions was also measured with the aim of underpinning the effect of coatings and presence of fluorides species on the cell response, the bulk material, and the coated alloy were studied using live/dead cell test, with the best results obtained for thinner fluoride containing coatings.

## Keywords

PEO; Mg alloys; Corrosion; Biodegradable materials.

## 1. Introduction

Magnesium (Mg) and its alloys show great potential as biodegradable implants, which eliminate the need of a second surgical procedure for implant removal [1, 2]. These materials have important advantages compared to both degradable polymers and other metallic implants, *e.g.*, 4-fold higher E-modulus, 3-fold higher tensile and yield strength in comparison with degradable polymers [3, 4], and similar mechanical properties to the real bone in contrast to titanium-based materials (Ti) or steel [5-7]. However, the degradation rate of magnesium based materials is still considered to be too high, leading to the loss of mechanical integrity and other problems like generation of hydrogen gas bubbles and local alkalization [8, 9]. With the aim to overcome this limitation, two main strategies are in the focus of research:

The first one is the design of new materials with desired composition and microstructure [10]. Using this approach, the earliest Mg based materials studies for biomedical applications were carried out on conventional magnesium alloys containing aluminium [11, 12]. However, aluminium is potentially toxic for the human body, therefore there is a growing interest in biodegradable magnesium alloys composed of non-toxic elements [13-15]. In particular, calcium (Ca) is considered as a good candidate because it plays a crucial role in the formation of human bone [16]. However, up to date, the degradation rate obtained for the Mg-Ca based systems is still too high to ensure a proper bone healing process [13].

The second strategy in order to increase the corrosion resistance of Mg-based materials is the application of surface treatments that can provide stability at the initial stages after implantation and then progressively degrade. Many coating techniques have been tested including chemical conversion, anodizing techniques, ion implantation, sol-gel coatings and spraying [17]. Among them, plasma electrolytic oxidation (PEO) is a flexible option allowing a wide variation of composition, microstructure, porosity, and roughness of the coatings through modification of the electrolyte and process parameters [18]. This technique involves polarization of the material under high voltages in an appropriate electrolyte, with the generation of a large number of short-lived microdischarges caused by dielectric breakdown and the formation of plasma discharges with the incorporation of species from the electrolyte [19, 20]. This last characteristic is particularly important for biomedical applications, offering the possibility to create in one step the bioactive surfaces (containing Ca and phosphorous (P)), that can promote cell adhesion/ proliferation. Since hydroxyapatite (HA, ($Ca_{10}(PO_4)_6(OH)_2$)) is the main inorganic compound of natural bone, some efforts have been undertaken to incorporate Ca and P in the form of HA. The improved bioactive properties of PEO coatings containing HA, are already well known for Ti substrates [21], including previous work of the authors [22], but in the case of Mg-based materials investigations are at an initial stage and most of the research is only focused on the evaluation of corrosion properties [23, 24].

In fact, only few studies have reported incorporation of Ca and P from the electrolyte into PEO coated Mg-based materials. In particular, amorphous Ca/P incorporation into PEO coatings [25-27] and formation of calcium sodium metaphosphate [23]. The information available on in-situ incorporation of HA is rather limited; for instance, Gnedenkov et al. achieved it on Mg-Mn-Ce alloy by PEO in calcium glycerophosphate electrolyte; they further used a polytetrafluoroethylene powder post-treatment to improve the corrosion resistance [28]. Usually, cathodic HA deposition post-treatments are employed to develop HA-containing PEO coatings on Mg-based materials [29, 30] with improved corrosion behaviour or bioactivity.

With respect to PEO of Mg-Ca alloys in particular, Gu et al. [31] developed silicate based coatings on Mg-Ca (1 wt.%) alloy and reported an improvement of the corrosion resistance in Hank's solution,  and a better cell adhesion, proliferation and differentiation due to a reduction of Mg ion release and pH variations in the culture medium. However, the possibility to enhance the bioactivity with tailored PEO coatings containing Ca and P on Mg-Ca alloys has not been explored.

In the present study, one step PEO coatings are developed on Mg-Ca (0.8 wt %.) alloy and the influence of the electrolyte (with and without fluorides species) on coating composition, morphology and cell response is evaluated. The effect of treatment time on long term corrosion behaviour of fluorine-containing coatings was also studied in comparison with the non-coated alloy.

## 2. Experimental procedure

### 2.1 Material

Mg 0.8wt.% Ca alloy (mass fraction: 0.61% Ca, 0.003% Fe, 0.0021% Cu, 0.0009% Ni, 0.023% Si %, 0.02%Al, 0.006%Zn, 0.05% Mn, 0.000039% Be, and Mg balance) was used as substrate.

Specimens of size $10 \times 10 \times 4\ \mathrm{mm}^3$, $20 \times 20 \times 4\ \mathrm{mm}^3$ and $60 \times 6 \times 4\ \mathrm{mm}^3$ for cell work, electrochemical tests and hydrogen measurements, respectively, were ground successively with SiC papers to P1200 grit size and cleaned with iso-propanol prior to PEO treatment.

### 2.2 PEO coatings

PEO treatments were carried out using alternating current (AC) voltage-controlled EAC-S2000 power supply (ET Systems electronic, Altlußheim, Germany) in electrolytes with and without fluorides species for different treatment times (Table 1). Square waveform with a peak to peak voltage of 490 V and direct current (DC) offset of 190 V, duty cycle 50%, frequency 50 Hz and a current density limit of 138 $\mathrm{mA/cm^2}$ were used. Specimens for cell tests and hydrogen measurements were coated entirely. Specimens for electrochemical measurements were coated on one side only, using an insulating Laquer 45 resin (MacDermid, Birmingham, UK) to define the working area.

## 2.3 Surface characterisation

For metallographic characterisation of Mg-0.8Ca alloy, samples were wet ground through successive grades of silicon carbide abrasive papers from P120 to P1200 (Struers GmbH, Hannover-Garbsen, Germany), followed by diamond finishing to 0.1 µm. A JEOL 2100 transmission electron microscope (TEM; Freising, Germany) operating at 200 kV and equipped with energy-dispersive X-ray (EDX) microanalysis facilities was used for characterisation of second phase particles. TEM specimens were prepared by ion milling disks with a diameter of 3 mm and 0.1 mm-thick in a Gatan PIPS system (Munich, Germany) with a small incident angle until perforation.

Samples were examined by both optical and scanning electron microscopy (SEM) using a JEOL JSM-6400 microscope (JEOL GmbH, Freising, Germany) equipped with Oxford Link energy dispersive X-ray (EDS) microanalysis hardware. EDS surface area analysis results are cited as an average of three measurements performed at different locations. The cross-sections of the coated materials were prepared by grinding the specimens through successive grades of SiC abrasive paper to P1200 followed by polishing with 1 µm diamond paste.

NanoscopeIIIaMultiMode scanning Kelvin probe force microscope (SKPFM, Veeco-Digital Instruments,USA) working in tapping mode was used to obtain surface potential maps of uncoated specimens polished to a 0.1 µm diamond finish. A silicon tip with a platinum coating of 20 nm thickness was used for simultaneous acquisition of topographic and surface potential images. The tip to sample distance was kept constant at 100 nm for acquisition of surface potential images.

Phase composition was examined by X-ray diffraction (XRD) using a Philips X'Pert diffractometer (Cu Kα = 1.54056 Å) (Almelo, Netherlands) at a scanning speed of 0.01° per second for a scan range of 2θ from 10° to 80°.

Coating thicknesses were measured by the eddy current method, using a Fischer ISOSCOPE FMP10 (Windsor, USA) portable instrument, taking the average of ten measurements with a standard deviation of ~0.5 μm and later confirmed with cross-sectional SEM.

## 2.4 Electrochemical measurements

Polarization and EIS electrochemical measurements were performed using an AUTOLAB-PGSTAT 30 computer-controlled potentiostat in simulated body fluid (SBF [32]) at 37±0.5ºC. A conventional three-electrode cell was used, employing a graphite counter electrode, a silver–silver chloride reference electrode (Ag/AgCl) with a potential of 0.210 V with respect to the standard hydrogen electrode (SHE) and the specimen as a working electrode with 1 $cm^2$ of exposed area.

Polarization measurements were obtained after 1 h of immersion at a scan rate of 0.3 mV $s^{-1}$, from −200 mV to +2000 mV relative to the open circuit potential (OCP) and with a maximum current density of 5 mA $cm^{-2}$. The corrosion potential ($E_{corr}$) and corrosion current density ($i_{corr}$) were measured to evaluate the corrosion properties of the materials. Corrosion current density was calculated using the cathodic Tafel slope. Electrochemical impedance spectroscopy (EIS) measurements, were also performed for immersion times ranging up to 6 weeks. A sinusoidal perturbation of 10 mV RMS amplitude with respect to OCP and a frequency sweep from 30 kHz to 0.01 Hz was applied. Repeatability was tested by measuring at least two specimens. The impedance spectra were analysed using ZView software (Solartron Analytical, UK), the goodness of fit of the spectra corresponded to chi-squared (square of the standard deviation between the original data and the calculated spectrum) values <0.01. The errors for the individual parameters of the equivalent electrical circuits were <10%.

## 2.5 Hydrogen evolution

Hydrogen evolution measurements were performed in 175 mL of simulated body fluid (SBF) solution at 37°C for up to 70 days of immersion using bar specimens with a size of 60×6×4 $mm^3$. In all immersion tests the non-coated electrical contact area of the PEO-coated specimens was protected with Laquer 45 resin. The corrosion rate was calculated from the total volume of hydrogen evolved during the test [33]. After the corrosion tests, the specimens were characterised with optical microscopy and SEM in order to investigate the morphology and composition of the corrosion products.

## 2.6. Fluoride release

Measurements of the release kinetics of fluoride ions were conducted after 5, 8, and 12 weeks of immersion in SBF at 37 ± 0.5 ºC using the bar specimens with a total area of 10.4 $cm^2$. The amounts of total fluoride ions released from materials were measured using a fluoride ion-selective electrode (ISE, Crison, Barcelona, Spain), consisting of a lanthanum fluoride monocrystal membrane doped with europium. The membrane potential difference generated in the selective electrode, based on the concentration of $F^-$ in the solution, was measured using a reference electrode of Ag / AgCl and pH meter GLP22 (Crison). The calibration curve (Potential, mV= (-340±2)-(57±3) log [33], $\mu g\ mL^{-1}$) was obtained using $F^-$ standards (100 ppb, 500 ppb, 1 ppm, 2.5 ppm, and 5 ppm) prepared from a fluoride standard of 100 μg/mL.

In order to unify the ionic strength and pH of the solutions for correct determination of fluoride concentration, 25 mL of $F^-$-containing SBF aliquots were mixed with 25 mL of TISAB solution (57 mL $L^{-1}$ acetic acid, 58 g $L^{-1}$ sodium chloride, 4 g $L^{-1}$ 1,2diaminocyclohexane-N,N,N',N'-tetraacetic acid in distilled water with pH 5.0-5.5 adjusted with 6M sodium hydroxide). Three potential measurements were conducted per time on each specimen.

## 2.7 Biological investigation

To avoid the medium contact with the non-coated electrical connection area of the PEO specimens this area was protected with silicone screws.

Human bone-derived cells (HBDC) isolation was performed on bone fragments obtained from total hip replacement and approved by the local ethical committee (Ethik-Kommission der Ärztekammer Hamburg, OB 007/05). Adapted from Gartland *et al*. [34], cancellous bone pieces of about 5 mm were cut and cultured in Dulbecco's modified eagle medium (DMEM) Glutamax-I (Invitrogen Corporation, Karlsruhe, Germany) supplemented with 10% foetal bovine serum (FBS, PAA Laboratories GmbH, Linz, Austria), 1% penicillin and streptomycin (Invitrogen Corporation, Karlsruhe, Germany) for about 10 days without medium change under cell culture conditions (5% $CO_2$, 20% $O_2$, 95% relative humidity, 37°C) in an incubator (Heraeus BB 6220; Thermo Scientific, Bonn, Germany). At visibility of outgrowing HBDC, the medium was changed every 3 days. Passaging was performed when cells achieved about 80% confluence. Cells in the 2nd passage were used for the experiments.

HBDC were seeded on the different specimen in a density of $10x\ 10^4$ cells / sample in 50 µL medium, in beforehand agarose (Merck KGaA, Darmstadt, Germany) coated 6-well plates (Greiner Bio-One GmbH, Frickenhausen, Germany). After 40 min adherence, 6 mL of cell specific medium was added. The cells were then further cultured for up to 3 days. On the 3rd day, cytocompatibility was assessed via LIVE/DEAD Cell Viability assay (Life technologies, Darmstadt, Germany) and SEM observations.

LIVE/DEAD Cell Viability assay staining solution was prepared by adding 4 µL calcein AM (LIVE - green) and 10 µL ethidium homodimer-1 (DEAD - red) to 10 mL of cell culture medium. The samples were first washed with cell culture medium to eliminate non-adherent cells, followed by immersion of each sample in 1.5 mL of staining solution, and incubating them under cell culture conditions. The staining solution was then replaced by cell culture medium and samples were visualized by fluorescence microscopy (TI-Eclipse, Nikon GmbH, Düsseldorf, Germany), the applied filters were FITC (Ex: 460-500 nm; Em: 510-560 nm; Mirror at 505 nm) and Texas red (Ex: 540-580nm; Em: 600-660; Mirror at 595 nm).

Previous SEM investigations (Leica EM CPD300, Leica Mikrosysteme Vertrieb GmbH, Wetzlar, Germany), samples were critically point dried in 2-propanol (Merck KGaA, Darmstadt, Germany) to preserve cell morphology. In brief, after a 2.5% glutaraldehyde (Merck KGaA, Darmstadt, Germany) fixation step, carriers were stained in 1% osmium tetroxide (Merck KGaA, Darmstadt, Germany) followed by an aqueous alcoholic dehydration row with 2-propanol.

## 3. Results and discussion

### 3.1 Characterisation

The SEM micrographs of Mg-Ca alloy in as cast condition are shown in Figure 1. The alloy reveals α-Mg primary dendrites and eutectic lamellar structure α-Mg/$Mg_2Ca$ which was identified by TEM (Fig. 2). These results are consistent with the Mg–Ca phase diagram and other works [35, 36].

Some information about the local nobility between constituents on a submicron scale was obtained using SKPFM [37] (Fig. 3 a-d). $Mg_2Ca$ phase presents a very small potential difference compared to the Mg matrix, suggesting that no coupling phenomenon will occur on the $Mg_2Ca$/α-Mg interface (Fig. 3 a,b). The information available in the literature about the electrochemical character of $Mg_2Ca$ phase is very limited and to the authors' knowledge, the values of the potential difference have not been previously reported. In fact, there are controversial results regarding the electrochemical activity of $Mg_2Ca$. Some works claim the anodic behaviour of $Mg_2Ca$ with respect to α-Mg matrix and suggest that the lamellar eutectic corrodes first to protect the α-Mg matrix [38, 39], while in others studies the opposite response was reported with a cathodic behaviour of the second phase ($Mg_2Ca$) and preferential dissolution of the α-matrix [17, 39]. These apparently contradictory results might be explained by the presence of impurities and matrix segregation. A systematic study using SKPFM and SEM/EDS would be necessary in order to confirm the influence of these parameters.

In addition to the eutectic phase, the alloy shows inclusions with higher potential differences (in the range of ~120-330 mV) compared to the matrix leading to localized corrosion susceptibility (Fig. 3 c-f). A more detailed analysis of these particles using SEM (Fig. 3 g, points 1 and 2) and EDS (Table 2) reveals that they contain impurities (Fe, Si), which is detrimental for the corrosion behaviour of Mg-based materials according to other works [40, 41]. As an example, in Mg-Al alloys, similar potentials differences (~ 300 mV) were found for intermetallics Al-Mn-(Fe) and these particles were proposed to be the principal sites of cathodic activity promoting the dissolution of the surrounding α-Mg grains [42].

Figure 4 shows the surface morphologies of PEO1-F, PEO2-F and PEO3 coatings. A typical morphology of PEO layer with numerous pores and cracks at the sites of the discharge channels can be observed, the pores are formed due to the gas evolution through the molten oxide material during the PEO process [20]. In particular for the coating developed in the electrolyte without fluorides, porosity and irregularities of the surface are more pronounced which is related to the individual and collective characteristics of the micro discharges that affect the thermal conditions of the treatment [43].

EDS analysis of a large area of PEO1-F shows a Ca/P surface ratio of ~1.4, which is close to that of stoichiometric hydroxyapatite (HA). PEO2-F reveals a slight higher ratio (~2.0) and PEO3 a very low ratio (~0.5) compared to HA. It is already known that apatite compounds improve the surface bioactivity and enable strong fixation of an implant to the host bone[44, 45]. In fact, in authors' previous work it was reported that for PEO coated Ti, an over ratio of Ca/P close to that of HA accelerated the initial cell response [46].

The cross sections of the coatings prepared at the different conditions are shown in Figure 5. The examination of the backscattered scanning electron (BSE) micrographs for PEO containing fluorides reveals relatively uniform coatings comprising an outer porous layer and a barrier layer adjacent to the substrate. For 420s of treatment in the electrolyte containing fluorides, the coating is about 50 ± 5 µm and with increase of the PEO time to 540s the thickness significantly increases up to 70 ± 5 µm. In the case of PEO3, formed in the electrolyte without fluorides species, the coating shows irregular thickness (6 ± 3 µm) and it is much thinner compared to the PEO developed in electrolytes with fluorides. This is in agreement with other works reporting that fluorides containing electrolytes enhance the growth rate of PEO films [47] and also can promote the formation of protective coatings with increased resistance to pitting corrosion and wear resistance [48].

According to EDS point analysis (Table 3), both coatings developed in electrolytes containing NaF reveal a Ca/P ratio close to HA in the outer part and this ratio decreases inwards so that the inner part is mainly composed of Mg, F and O. The coating formed in the electrolyte without fluorides (PEO3) reveals a very low Ca/P ratio along the thickness of the coating.

XRD examination of PEO coatings formed in the electrolyte with fluorides, shows peaks corresponding to the substrate (Mg) and the formation of crystalline phases MgO, $MgF_2$, $CaF_2$, $Ca_5(PO_4)_3OH$ and $Mg_2(PO_4)F$ (Fig. 6). In the particular case of PEO2-F peaks of fluorapatite ($Ca_5(PO_4)_3F$) are also detected, which is in concordance with previous studies of bioactive PEO coatings developed on AM50 Mg alloy [49]. The fact longer PEO treatment time (thicker PEO coating) leads to the formation of fluorapatite phase is related to the discharge evolution during PEO process that determine parameters (temperature and cooling rate) which are critical for the different apatite-based materials microstructure [50].

The presence of MgO is due to the oxidation of the substrate, whereas the formation of $MgF_2$, $CaF_2$, $Ca_5(PO_4)_3OH$, and $Mg_2(PO_4)F$ are associated with the chemical reactions during the microdischarges between the electrolyte ions and the substrate. The detection of hydroxyapatite ($Ca_5(PO_4)_3OH$) and fluorapatite ($Ca_5(PO_4)_3F$) suggests that coatings would have the ability to promote the osseointegration between the implant and the bone. However, for the coating formed in the electrolyte without fluorides (PEO3), no crystalline Ca and/or P containing phases are observed and only peaks corresponding to Mg substrate and the oxide layer (MgO) are detected suggesting lower potential bioactive properties for this layer.

### 3.2 Influence of the coating microstructure and effect of fluorides on cell behaviour

In order to evaluate the effect of fluorides PEO1-F was selected for the cell studies out of the two coatings containing fluorides. The selection was justified by the shorter treatment time, hence, a lower energy consumption and lower cost of PEO1-F fabrication. For further work, it would be interesting to analyse the effect of composition and microstructure of different PEO coatings containing fluorides in order to observe modifications on the cell behaviour.

However, as a first approximation, the present works aims just to compare the cell colonization with and without presence of fluorides.

Cell spreading is an important event for an adherent cell, and it precedes cell proliferation.

The live-dead staining images obtained after 3 days of immersion of the substrate (Mg-0.8Ca) and PEO3 coating reveal round shape cells and high gas production, indicating a low cell adhesion and proliferation (Fig 7 a,b). However, for the particular case of PEO1-F is observed a higher number of cells after the same immersion time showing a good adhesion and flat shape, which indicates an improvement of the surface bioactivity (Fig 7 c).

The SEM micrograph corresponding to the cell spreading on PEO1-F (Fig. 7 f) shows much flatter cell morphology than on the substrate and PEO3 (Fig. 7 d,e). The better colonization found for PEO1-F might be related to the stability of the coating that allows cell to grow into the micropores, which has been reported to be beneficial for cell growing and proliferation [46].

## 3.3 Corrosion behaviour of selected coatings

Cell behaviour results show a clear improvement of cell response for fluoride-containing PEO in comparison to the one produced in F-free electrolyte. Based on those results, the two coatings containing fluorides (PEO1-F and PEO2-F) were selected to evaluate the influence of the coating thickness on corrosion behaviour in comparison with the bare substrate.

### *3.3.1 DC polarization results*

Potentiodynamic polarization curves after 1 hour of immersion in SBF at 37°C are plotted in Figure 8 for the studied materials (bare substrate, PEO1-F and PEO2-F).

The curves for both coatings shifted to more noble corrosion potential and to lower current densities (0.94 $\mu$A $cm^{-2}$ for PEO1-F, 1.0 $\mu$A $cm^{-2}$ for PEO2-F, 465 $\mu Acm^{-2}$ for substrate) indicating their higher electrochemical stability. The better stability of both PEO coatings is also suggested by a passive region starting at about -1.6 $V_{Ag/AgCl}$. In the particular case of PEO1-F, the coating shows a slightly lower passive current (3 μA $cm^{-2}$) and more positive corrosion potential (-1.65 $V_{Ag/AgCl}$) compared to PEO2-F ($i_{pass}$= 10 μA $cm^{-2}$, $E_{corr}$= -1.85$V_{Ag/AgCl}$). For most protective coatings, thicker layers impede the penetration of the electrolyte and therefore delay the corrosion process. However, in the particular case of PEO coatings on Mg alloys, controversial results have been found about the influence of coating thickness on the corrosion behaviour, which arise mainly from electrical regimes and parameters used to develop the coatings [23, 51]. Longer treatment time, higher voltages or current of PEO processing lead to thicker coatings but also to the formation of strong microdischarges which have been reported as detrimental for the barrier properties of the oxide layer [52].

### *3.3.2 Electrochemical impedance spectroscopy*

Figure 9 shows Nyquist and Bode diagrams of the EIS data (experimental and fitted) for the substrate and PEO coatings containing fluorides, up to 4 weeks of immersion in SBF solution at 37 ºC.

For the substrate, the equivalent circuit shown in Figure 10 a was used to fit the experimental data, where $R_e$ represents the resistance of the electrolyte, $R_{cp}$/$CPE_{cp}$ describe the resistance and the capacitive behaviour of the corrosion products formed on the alloy surface. The charge transfer resistance and the capacitance of the double layer are represented by $R_{ct}$ and $CPE_{dl}$ corresponding to the electrochemical activities in the substrate /electrolyte interface. Constant Phase Elements (CPE) were used instead of capacitances in order to account for non-ideal behaviour of the system. The impedance of a CPE is calculated as $Z = 1 / [CPE (j\omega)^n]$; where ω is radial frequency, n is the exponential factor ($-1 \leq n \leq 1$) and $j = \sqrt{-1}$ is the imaginary number. CPE corresponds to a numerical value of admittance of the system, 1/Z, at $\omega = 1$ rad $s^{-1}$. With $n = 1$, constant phase element becomes an ideal capacitor.

Figure 9 a shows the typical impedance response for Mg alloys [53]. After 1 h of immersion, there are two relaxation processes (associated with the presence of corrosion products and the electrochemical activities), but in some cases they are difficult to distinguish due to a strong overlapping. With increase of the immersion time (28 d), a new response appears at low frequencies. In some works it has been ascribed to an inductive behaviour due to the presence of absorbed species on the metal surface or to the dissolution of the semi-passive corrosion product film [54]. However, in this range of frequencies it is often impossible to maintain stationary conditions for Mg based materials and therefore in the present work this part of the spectra was not used to obtain the fittings.

As observed in the Bode plot (Figure 9 b), the modulus of the impedance reaches a maximum in almost full frequency range after 3 d of immersion and decreases afterwards. This behaviour is associated to the formation of a semi protective corrosion product film after 3 d of immersion and its partial breakdown with time [55]. This tendency has already been reported by other authors; for instance, Li [56] recently observed a similar response in as-cast AZ63 magnesium alloy after 12 h immersion in 3.5 wt. % in NaCl and Ahmadkhaniha [57] on as-cast pure Mg and on Magnesium–hydroxyapatite composite after immersion up to 4 days in Dulbecco’s phosphate buffered saline solution.

For coated specimens, (PEO1-F and PEO2-F) the proposed equivalent circuits used to fit the experimental data are shown in Fig. 10 b-d depending on the immersion time. For initial stages of immersion (Fig. 10 b), the time constant observed at high frequency ($10^4$ Hz) can be ascribed to the response of the outer porous part of the coating ($R_{out}$/$CPE_{out}$) whereas the time constant at lower frequencies (1 Hz) is related to the PEO inner barrier layer ($R_{in}$/$CPE_{in}$).

With the increase of the immersion time (3 d), the electrolyte penetrates the coating with the consequent chemical degradation of the latter. The time constant ascribed to the outer porous layer practically disappears and the coatings show a combined response of the two PEO layers (outer and inner) that is represented by the $R_{coat}$/$CPE_{coat}$. New relaxation processes appear at low frequencies (0.1 Hz) which are associated with the electrochemical activity on the metal/electrolyte interface. After 28 days of immersion, a third time constant can be identified at low-medium frequencies, although it is difficult to distinguish due to a strong overlapping, which accounts for the contribution of the corrosion products entrapped between the substrate and the coating. In addition, slight differences in the time constant at high frequencies for coatings containing fluorides may be related with the partial sealing of the outer part with corrosion products that block the porosity; this effect appears more pronounced in the case of PEO1-F.

Therefore, three different equivalent circuits were used to fit the experimental data depending on the exposure time. A two time constant circuit is used after 1 h (Fig. 10 b), 3 and 7 d, (Fig. 10 c) and a three time constant circuit after 28 d (Fig. 10 d).

To analyse the evolution of the coating corrosion resistance with time, $R_{coat}$, $R_{cp}$ and $R_{ct}$ are represented (Fig. 11). For short times of immersion (1h) and for both materials, the values of $R_{in}$ are in the range of $7\times10^4$-$10^5\Omega$ cm$^2$ and $R_{out}$ $2\times10^3$-$3\times10^3\Omega$ cm$^2$ which agree with previous research [58]. After 3 d of immersion the outer layer resistance diminishes abruptly that is why the contribution of both inner and outer part of the PEO coating are evaluated together as the coating resistance ($R_{coat}$). In Figure 11 a it can be observed that $R_{coat}$ and $R_{ct}$ values of both coatings tend to diminish with the immersion time. This progressive diminution indicates that the properties of the barrier layer start to degenerate as a consequence of the electrolyte uptake, which over time (28 d) results in the precipitation of corrosion products in the interface substrate/coating. The latter was also observed by Córdoba [59] who evaluated the corrosion resistance in SBF of polymeric coatings formed on pretreated AZ31 and ZE41 magnesium alloys. However, they evaluated the contribution of the corrosion products together with the influence of an interfacial layer of $MgF_2$ formed during the pretreatment in hydrofluoric acid; this initial layer degrades with time resulting in the formation of corrosion products.

These values are slightly lower for PEO2-F (Fig. 11 b) which indicates the lower corrosion resistance of the latter as previously deduced from the potentiodynamic tests.

### *3.3.3 Hydrogen evolution measurements*

Figure 12 shows the hydrogen volume and the hydrogen evolution rate versus time for the studied materials, along with their macro-appearance, up to 10 weeks of immersion in SBF at 37ºC. The cross-sections of the specimens after immersion 4 and 8 weeks are given in Figure 13.

As expected, the uncoated material shows initially high amount of hydrogen with an evolution rate of ~2.8mL $cm^{-2}$ $d^{-1}$ after 1 day, which progressively decreases to ~1.3 mL $cm^{-2}$ $d^{-1}$ and ~ 1.1 mL $cm^{-2}$ $d^{-1}$ after 4 and 6 weeks of immersion, respectively. A steady-state corrosion rate is observed between weeks 6 and 10 of immersion. The subsequent decrease in the corrosion rate with time may be associated with the formation of a corrosion products layer that can partially protect the material. This hypothesis is confirmed by the SEM images of cross sections of the material after 4 and 8 weeks of immersion, revealing a homogeneous corrosion layer covering the surface (Fig. 13 a,b). However, the presence of cracks in the formed oxide layer provides paths for the chloride-containing solution to the substrate leading to both general and localised corrosion processes. The last one appears with the immersion time and results in loss of material around the specimen perimeter and shape distortion, as can be observed in the digital image of the substrate after 10 weeks of immersion in SBF at 37 ºC (Fig. 12 c).

A previous work on Mg-Ca systems (0.5-10 wt% Ca) reported that for Ca concentration below 1.25 wt.% the corrosion process is driven by a general corrosion mechanism which turns into localised for higher concentration due to a severe electrochemical activity [60]. The results obtained in this work for the Mg-0.8wt%Ca alloy, suggest that the second phase $Mg_2Ca$ does not play an important role as starting point for microgalvanic activities and the localised phenomena, which appear with time, are associated with the impurities present in the alloy. This key role of impurities on the corrosion of Mg-Ca alloys is in accordance with previous research on other Mg-based materials [40, 61].

Both PEO coatings showed similar behaviour and considerably reduced hydrogen evolution rate during first 2 weeks of immersion (~0.1mL $cm^{-2}$ $d^{-1}$). After this period, an increase can be observed (up to 0.4mL $cm^{-2}$ $d^{-1}$ after 10 weeks of immersion) which is related to the loss of protective properties of the inner PEO layer and the starting of the electrochemical activities in the interface substrate/coating (Fig. 13 b) [25, 29, 62]. In fact, after 6 weeks of immersion the coated alloy reaches approximately the same corrosion rate as the non-coated one. After 4 weeks of immersion PEO1-F do not show any sign of localised corrosion whereas for the coating PEO2-F the localised process has already started (Fig. 13 c,e). This slightly better behaviour of the thinner PEO coating (developed under shorter process time) is associated with its greater compactness and smaller size of inner voids compared with the thicker coating (Fig. 5 a,c), which are related to the individual and collective characteristics of the micro-discharges generated during PEO process. These micro-discharges directly affect the microstructure, morphology and phase formation of the coating and they become stronger with time, which has been reported to have a negative effect on the coatings in some cases

[43]. For longer immersion time in SBF (8 weeks) both coatings are characterised by localised corrosion as it has been reported before for this type of coatings, in particular covering Mg alloys [63, 64]. Regarding the mechanism of the localised attack, Liu et al. claim that the corrosion products formed and accumulated in the interface substrate/coatings cause stress and damage the PEO coating. In another work, Gao et al. [23] proposed a more detail mechanism for this phenomenon based on the gas (hydrogen) produced during the cathodic reaction of the Mg matrix corrosion process. At some point, the hydrogen pressure would eventually become sufficient to cause the coating to blister and /or break.

The macro appearance of the PEO specimens containing fluorides after 10 weeks of immersion in SBF at 37 ºC (Fig. 12 c) reveal clear signs of corrosion with a clear localised attack.

### *3.3.4 Fluoride ions release for PEO coatings containing fluorides*

Figure 14 shows $F^-$ ion release of studied materials following immersion in SBF for 5, 8 and 12 weeks.

A different tendency can be observed due to the influence of the coating thickness and composition on the mechanism and level of the $F^-$ ion release, which has been related to the different extent of crystallinity of the fluoride-containing compounds and the amount of fluorine in the coatings. There is ~11 at.% and ~23 at.% of F in PEO1-F and PEO2-F, respectively (Table 2); further, the PEO2-F coating formed for longer time, reveals greater peak intensities for $MgF_2$ and $Mg_2(PO_4)F$.

For PEO1-F, the ion release slightly increases with time from 224.6 μg $cm^{-2}$ to 336.5 μg $cm^{-2}$ after 5 and 12 weeks of immersion respectively. It should be considered that the liberated fluoride will react with Ca and Mg ions of the SBF, precipitating $CaF_2$ and $MgF_2$, i.e. the ISE detects only the remaining free excess of $F^-$ in the solution. In accordance with the molar concentrations of $Ca^{2+}$ and $Mg^{2+}$ available in the SBF, a maximum of 8.4 mM of liberated $F^-$ can be bound as precipitates. According to the solubility products, $K_{sp}$, of $CaF_2$ and $MgF_2$ ($3.9\times10^{-11}$ and $5.16\times10^{-11}$, respectively) the dissolution of these precipitates will produce 0.9 mM of free $F^-$ maximum. For comparison, the concentration of free $F^-$ during immersion of PEO1-F increased from 0.7 mM to 1.05 mM. The increasing amount of detected fluoride suggests that not all the soluble reserves of fluoride compounds present in the coating were released during 12 weeks of immersion in SBF at 37 ºC, i.e. the coating continues to supply $F^-$. It is clear that the 0.7 mM (or 224.6 μg $cm^{-2}$) is the actual released amount after 5 weeks (since it is lower than the solubility limit of 0.9 mM), and the 1.05 mM (336.5 μg $cm^{-2}$) release after 12 weeks corresponds to a lower limit (with extra released $F^-$ being bound into $CaF_2$ and $MgF_2$). However, in the case of PEO2-F the amount of fluorides release to the media decreases with the immersion time from 379 μg $cm^{-2}$ (1.19 mM in the SBF) to 59.5 μg $cm^{-2}$ (0.19 mM) after 5 and 12 weeks of immersion respectively, which means that the source of fluoride is being depleted. Additionally, the coatings are liberating $Mg^{2+}$ during corrosion and, possibly, $Ca^{2+}$ which also contribute to the $F^-$ equilibrium. This behaviour seems to be in agreement with the XRD and EDX results which show higher intensity of the crystalline fluoride-containing compounds ($CaF_2$, $MgF_2$, $Ca_5(PO_4)_3F$ y $Mg_2(PO_4)F$ for PEO2-F, and higher content of fluorine in PEO1-F.

Another aspect to consider is the impact that the inadequate fluoride concentration can have on the biological processes. The world health organization (WHO) recommends a $F^-$ content in water for consumption not more than 0.7 - 1.2 mg $L^{-1}$, the optimal consumption amount for an adult (depending of the weight) being 1.4-3.4 mg $d^{-1}$, from which 50% is excreted by the kidneys and the rest remains in bones, teeth and organs. Therefore, the average fluoride concentration in human blood plasma is 1 μmol $L^{-1}$ = 19 ppb. In adults with endemic fluorosis the $F^-$ levels can achieve values from 30 to 80 μmol / L, and a poisoning effect for humans is found in concentrations of between 500-780 μmol $L^{-1}$ [65] .

In the present study, the highest level of $F^-$ release into SBF was 379.6 μg $cm^{-2}$ for PEO2-F after 5 weeks of immersion. Considering an implant with an area of 10 $cm^2$ and a blood volume of 5 L the amount of $F^-$ ion release rate would be ~10 ppb $d^{-1}$, which is far below any poisoning concentrations. Further studies should be conducted in order to evaluate other advantages of $F^-$ presence, like the antibacterial effect.

## Conclusions

- PEO coatings without and with fluoride compounds were generated on Mg-0.8 wt%Ca alloy. The addition of fluorides into the electrolyte improves the growth rate of PEO coatings and promotes the incorporation of Ca and P with formation of $Ca_5(PO_4)_3OH$, $Ca_5(PO_4)_3F$ and $Mg_2(PO_4)F$ compounds.

- PEO1-F shows better bioactivity compared to PEO3 without fluorides, with a higher number of cells well bonded to the PEO surface after the same immersion time. This difference is related to different corrosion protection properties of the formed layers. The F-free coating is not able to ensure sufficient delay of corrosion and does not provide suitable conditions for cell attachment and growth.

- Corrosion studies (hydrogen evolution, potentiodynamic polarisation, and electrochemical impedance spectroscopy) prove a clear improvement of the corrosion resistance for specimens with fluoride-containing coatings. The thinner coating (PEO1-F) reveals a slightly better behaviour which may be related to the individual and collective characteristics of the micro-discharges generated during PEO process. The composition and porosity of the formed layers can have a significant effect on their conversion during the degradation process.

- The F$^-$ release into SBF was the highest (379.6 μg cm$^{-2}$ or 1.19 ppm) for PEO2-F after 5 weeks of immersion, but the coating was depleted as F$^-$ source by week 12. The PEO1-F coating continued to supply F$^-$ increasingly, reaching 336.5 μg cm$^{-2}$ or 1.05 ppm by the 12th week of immersion. In all cases the released amount of F$^-$ can be considered well within the limits safe for human consumption.

## Acknowledgments

This work was partially supported by MULTISURF (Marie Skłodowska-Curie grant agreement No 645676) European project and Multimat Challenge Programme (S2013/MIT-2862-CM via Regional Government of Madrid and EU Structural Funds). MM is grateful to the Juan de la Cierva Programme (MICINN, Spain, IJCI-2014-19117) and Alexander von Humboldt Foundation, Germany. The technical support of Mr. U. Burmester and Mr. V. Heitmann is gratefully acknowledged. EM is grateful to the Ramon y Cajal Programme (MICINN, Spain, RYC-2010-06749).

## References

[1] Y. Chen, Z. Xu, C. Smith, J. Sankar, Recent advances on the development of magnesium alloys for biodegradable implants, Acta Biomater., 10 (2014) 4561-4573.
[2] G. Song, Control of biodegradation of biocompatable magnesium alloys, Corros. Sci., 49 (2007) 1696-1701.
[3] L. Claes, Mechanical characterization of biodegradable implants, Clin. Mater., 10 (1992) 41-46.
[4] F. Witte, V. Kaese, H. Haferkamp, E. Switzer, A. Meyer-Lindenberg, C. Wirth, H. Windhagen, In vivo corrosion of four magnesium alloys and the associated bone response, Biomaterials, 26 (2005) 3557-3563.
[5] N.-E.L. Saris, E. Mervaala, H. Karppanen, J.A. Khawaja, A. Lewenstam, Magnesium: an update on physiological, clinical and analytical aspects, Clin. Chim. Acta, 294 (2000) 1-26.
[6] G.-L. Song, Corrosion prevention of magnesium alloys, Elsevier, 2013.
[7] M.P. Staiger, A.M. Pietak, J. Huadmai, G. Dias, Magnesium and its alloys as orthopedic biomaterials: a review, Biomaterials, 27 (2006) 1728-1734.
[8] W.-D. Mueller, M.L. Nascimento, M.F.L. De Mele, Critical discussion of the results from different corrosion studies of Mg and Mg alloys for biomaterial applications, Acta Biomater., 6 (2010) 1749-1755.
[9] S. Virtanen, Biodegradable Mg and Mg alloys: Corrosion and biocompatibility, Mater. Sci. Eng., B, 176 (2011) 1600-1608.
[10] M. Niinomi, M. Nakai, J. Hieda, Development of new metallic alloys for biomedical applications, Acta Biomater., 8 (2012) 3888-3903.
[11] Z. Wen, C. Wu, C. Dai, F. Yang, Corrosion behaviors of Mg and its alloys with different Al contents in a modified simulated body fluid, J. Alloys Compd., 488 (2009) 392-399.
[12] Y. Zong, G. Yuan, X. Zhang, L. Mao, J. Niu, W. Ding, Comparison of biodegradable behaviors of AZ31 and Mg–Nd–Zn–Zr alloys in Hank's physiological solution, Mater. Sci. Eng., B, 177 (2012) 395-401.
[13] Z. Li, X. Gu, S. Lou, Y. Zheng, The development of binary Mg–Ca alloys for use as biodegradable materials within bone, Biomaterials, 29 (2008) 1329-1344.

[14] E. Zhang, L. Yang, J. Xu, H. Chen, Microstructure, mechanical properties and bio-corrosion properties of Mg–Si (–Ca, Zn) alloy for biomedical application, Acta Biomater., 6 (2010) 1756-1762.
[15] S. Zhang, X. Zhang, C. Zhao, J. Li, Y. Song, C. Xie, H. Tao, Y. Zhang, Y. He, Y. Jiang, Research on an Mg–Zn alloy as a degradable biomaterial, Acta Biomater., 6 (2010) 626-640.
[16] S. Shadanbaz, G.J. Dias, Calcium phosphate coatings on magnesium alloys for biomedical applications: a review, Acta Biomater., 8 (2012) 20-30.
[17] H. Hornberger, S. Virtanen, A. Boccaccini, Biomedical coatings on magnesium alloys–a review, Acta Biomater., 8 (2012) 2442-2455.
[18] C. Blawert, S. Sah, N. Scharnagl, M.B. Kannan, Plasma electrolytic oxidation/micro-arc oxidation of magnesium and its alloys, Surface Modification of Magnesium and its Alloys for Biomedical Applications: Modification and Coating Techniques, (2015) 193.
[19] R. Arrabal, E. Matykina, T. Hashimoto, P. Skeldon, G. Thompson, Characterization of AC PEO coatings on magnesium alloys, Surf Coat Technol, 203 (2009) 2207-2220.
[20] A. Yerokhin, X. Nie, A. Leyland, A. Matthews, S. Dowey, Plasma electrolysis for surface engineering, Surf Coat Technol, 122 (1999) 73-93.
[21] S. Gnedenkov, Y.P. Scharkeev, S. Sinebryukhov, O. Khrisanfova, E. Legostaeva, A. Zavidnaya, I. Khlusov, Formation and properties of bioactive surface layers on titanium, Inorg. Mater. Appl. Res., 2 (2011) 474-481.
[22] M. Mohedano, R. Guzman, R. Arrabal, J.L. López Lacomba, E. Matykina, Bioactive plasma electrolytic oxidation coatings—The role of the composition, microstructure, and electrochemical stability, J. Biomed. Mater. Res. Part B Appl. Biomater., 101 (2013) 1524-1537.
[23] Y. Gao, A. Yerokhin, A. Matthews, Effect of current mode on PEO treatment of magnesium in Ca-and P-containing electrolyte and resulting coatings, Appl. Surf. Sci., 316 (2014) 558-567.
[24] L. White, Y. Koo, S. Neralla, J. Sankar, Y. Yun, Enhanced mechanical properties and increased corrosion resistance of a biodegradable magnesium alloy by plasma electrolytic oxidation (PEO), Mater. Sci. Eng., B, 208 (2016) 39-46.
[25] Y. Gao, A. Yerokhin, A. Matthews, DC plasma electrolytic oxidation of biodegradable cp-Mg: In-vitro corrosion studies, Surface and Coatings Technology, 234 (2013) 132-142.
[26] P.B. Srinivasan, J. Liang, C. Blawert, M. Störmer, W. Dietzel, Characterization of calcium containing plasma electrolytic oxidation coatings on AM50 magnesium alloy, Appl. Surf. Sci., 256 (2010) 4017-4022.
[27] Z. Yao, L. Li, Z. Jiang, Adjustment of the ratio of Ca/P in the ceramic coating on Mg alloy by plasma electrolytic oxidation, Appl. Surf. Sci., 255 (2009) 6724-6728.
[28] S. Gnedenkov, S. Sinebryukhov, A. Zavidnaya, V. Egorkin, D. Mashtalyar, V. Sergienko, A. Yerokhin, A. Matthews, Composite hydroxyapatite–PTFE coatings on Mg–Mn–Ce alloy for resorbable implant applications via a plasma electrolytic oxidation-based route, J. Taiwan Inst. Chem. Eng., 45 (2014) 3104-3109.
[29] Y. Gao, A. Yerokhin, A. Matthews, Deposition and evaluation of duplex hydroxyapatite and plasma electrolytic oxidation coatings on magnesium, Surface and Coatings Technology, 269 (2015) 170-182.
[30] Y. Gao, A. Yerokhin, A. Matthews, Mechanical behaviour of cp-magnesium with duplex hydroxyapatite and PEO coatings, Materials Science and Engineering: C, 49 (2015) 190-200.
[31] X. Gu, N. Li, W. Zhou, Y. Zheng, X. Zhao, Q. Cai, L. Ruan, Corrosion resistance and surface biocompatibility of a microarc oxidation coating on a Mg–Ca alloy, Acta Biomater., 7 (2011) 1880-1889.
[32] A. Oyane, H.M. Kim, T. Furuya, T. Kokubo, T. Miyazaki, T. Nakamura, Preparation and assessment of revised simulated body fluids, J Biomed Mater Res A, 65 (2003) 188-195.
[33] G. Song, A. Atrens, D. StJohn, An hydrogen evolution method for the estimation of the corrosion rate of magnesium alloys, Magnesium Technology 2001, (2001) 254-262.
[34] A. Gartland, R.M. Rumney, J.P. Dillon, J.A. Gallagher, Isolation and culture of human osteoblasts, Human Cell Culture Protocols, (2012) 337-355.
[35] N.T. Kirkland, N. Birbilis, J. Walker, T. Woodfield, G.J. Dias, M.P. Staiger, In vitro dissolution of magnesium–calcium binary alloys: clarifying the unique role of calcium additions in bioresorbable magnesium implant alloys, J. Biomed. Mater. Res. Part B Appl. Biomater., 95 (2010) 91-100.
[36] M. Mezbahul-Islam, A.O. Mostafa, M. Medraj, Essential magnesium alloys binary phase diagrams and their thermochemical data, Journal of Materials, 2014 (2014).

[37] M. Jönsson, The Atmospheric Corrosion of Magnesium Alloys: Influence of Microstructure and Environments, (2007).

[38] H. Bakhsheshi-Rad, M. Abdul-Kadir, M. Idris, S. Farahany, Relationship between the corrosion behavior and the thermal characteristics and microstructure of Mg–0.5 Ca–xZn alloys, Corros. Sci., 64 (2012) 184-197.

[39] J. Yang, J. Peng, E.A. Nyberg, F.-s. Pan, Effect of Ca addition on the corrosion behavior of Mg–Al–Mn alloy, Appl. Surf. Sci., 369 (2016) 92-100.

[40] O. Lunder, K. Nisancioglu, R.S. Hansen, Corrosion of die cast magnesium-aluminum alloys, in, SAE Technical Paper, 1993.

[41] S. Mathieu, C. Rapin, J. Steinmetz, P. Steinmetz, A corrosion study of the main constituent phases of AZ91 magnesium alloys, Corros. Sci., 45 (2003) 2741-2755.

[42] G. Williams, H. ap Llwyd Dafydd, R. Grace, The localised corrosion of Mg alloy AZ31 in chloride containing electrolyte studied by a scanning vibrating electrode technique, Electrochim. Acta, 109 (2013) 489-501.

[43] V. Dehnavi, B.L. Luan, X.Y. Liu, D.W. Shoesmith, S. Rohani, Correlation between plasma electrolytic oxidation treatment stages and coating microstructure on aluminum under unipolar pulsed DC mode, Surf Coat Technol, 269 (2015) 91-99.

[44] K. Kuroda, M. Okido, Hydroxyapatite coating of titanium implants using hydroprocessing and evaluation of their osteoconductivity, Bioinorganic chemistry and applications, 2012 (2012).

[45] S.-H. Lee, H.-W. Kim, E.-J. Lee, L.-H. Li, H.-E. Kim, Hydroxyapatite-TiO2 hybrid coating on Ti implants, J. Biomater. Appl., 20 (2006) 195-208.

[46] M. Mohedano, E. Matykina, R. Arrabal, A. Pardo, M. Merino, Metal release from ceramic coatings for dental implants, Dent. Mater., 30 (2014) e28-e40.

[47] F. Liu, J. Yu, Y. Song, D. Shan, E.-H. Han, Effect of potassium fluoride on the in-situ sealing pores of plasma electrolytic oxidation film on AM50 Mg alloy, Mater. Chem. Phys., 162 (2015) 452-460.

[48] B. Kazanski, A. Kossenko, M. Zinigrad, A. Lugovskoy, Fluoride ions as modifiers of the oxide layer produced by plasma electrolytic oxidation on AZ91D magnesium alloy, Appl. Surf. Sci., 287 (2013) 461-466.

[49] E. Matykina, I. Garcia, R. Arrabal, M. Mohedano, B. Mingo, J. Sancho, M. Merino, A. Pardo, Role of PEO coatings in long-term biodegradation of a Mg alloy, Appl. Surf. Sci., 389 (2016) 810-823.

[50] I. Denry, J. Holloway, P. Gupta, Effect of crystallization heat treatment on the microstructure of niobium- doped fluorapatite glass- ceramics, J. Biomed. Mater. Res. Part B Appl. Biomater., 100 (2012) 1198-1205.

[51] F. Jaspard-Mecuson, T. Czerwiec, G. Henrion, T. Belmonte, L. Dujardin, A. Viola, J. Beauvir, Tailored aluminium oxide layers by bipolar current adjustment in the Plasma Electrolytic Oxidation (PEO) process, Surf Coat Technol, 201 (2007) 8677-8682.

[52] F. Mécuson, T. Czerwiec, T. Belmonte, L. Dujardin, A. Viola, G. Henrion, Diagnostics of an electrolytic microarc process for aluminium alloy oxidation, Surf Coat Technol, 200 (2005) 804-808.

[53] W. Liu, F. Cao, A. Chen, L. Chang, J. Zhang, C. Cao, Corrosion behaviour of AM60 magnesium alloys containing Ce or La under thin electrolyte layers. Part 1: Microstructural characterization and electrochemical behaviour, Corros. Sci., 52 (2010) 627-638.

[54] R.M. Asmussen, W.J. Binns, P. Jakupi, D. Shoesmith, Microstructural Effects on Corrosion of AM50 Magnesium Alloys, J. Electrochem. Soc., 161 (2014) C501-C508.

[55] S. Mathieu, C. Rapin, J. Hazan, P. Steinmetz, Corrosion behaviour of high pressure die-cast and semi-solid cast AZ91D alloys, Corros. Sci., 44 (2002) 2737-2756.

[56] J. Li, Q. Jiang, H. Sun, Y. Li, Effect of heat treatment on corrosion behavior of AZ63 magnesium alloy in 3.5 wt.% sodium chloride solution, Corros. Sci., 111 (2016) 288-301.

[57] D. Ahmadkhaniha, M. Fedel, M.H. Sohi, A.Z. Hanzaki, F. Deflorian, Corrosion behavior of magnesium and magnesium–hydroxyapatite composite fabricated by friction stir processing in Dulbecco's phosphate buffered saline, Corros. Sci., 104 (2016) 319-329.

[58] R. Arrabal, J.M. Mota, A. Criado, A. Pardo, M. Mohedano, E. Matykina, Assessment of duplex coating combining plasma electrolytic oxidation and polymer layer on AZ31 magnesium alloy, Surface and Coatings Technology, 206 (2012) 4692-4703.

[59] L. Córdoba, M. Montemor, T. Coradin, Silane/TiO 2 coating to control the corrosion rate of magnesium alloys in simulated body fluid, Corros. Sci., 104 (2016) 152-161.

[60] H.R.B. Rad, M.H. Idris, M.R.A. Kadir, S. Farahany, Microstructure analysis and corrosion behavior of biodegradable Mg–Ca implant alloys, Materials & Design, 33 (2012) 88-97.

[61] G. Ballerini, U. Bardi, R. Bignucolo, G. Ceraolo, About some corrosion mechanisms of AZ91D magnesium alloy, Corros. Sci., 47 (2005) 2173-2184.

[62] R. Arrabal, E. Matykina, F. Viejo, P. Skeldon, G. Thompson, Corrosion resistance of WE43 and AZ91D magnesium alloys with phosphate PEO coatings, Corros. Sci., 50 (2008) 1744-1752.

[63] R. Arrabal, A. Pardo, M. Merino, M. Mohedano, P. Casajús, E. Matykina, P. Skeldon, G. Thompson, Corrosion behaviour of a magnesium matrix composite with a silicate plasma electrolytic oxidation coating, Corros. Sci., 52 (2010) 3738-3749.

[64] W. Zhang, B. Tian, K.-Q. Du, H.-X. Zhang, F.-H. Wang, Preparation and corrosion performance of PEO coating with low porosity on magnesium alloy AZ91D in acidic KF system, Int. J. Electrochem. Sci, 6 (2011) 5228-5248.

[65] N.I. Agalakova, G.P. Gusev, Molecular mechanisms of cytotoxicity and apoptosis induced by inorganic fluoride, ISRN Cell Biology, 2012 (2012).

## Tables

**Table 1.** Parameters of the different PEO treatments.

**Table 2**. EDS point analysis of Figure 3 g point1 and 2.

**Table 3.** EDS analysis of the coatings.

## Figures

**Figure 1.** SEM micrographs of Mg-Ca alloy in as cast condition (a) Lower magnification (b) Higher magnification.

**Figure 2.** TEM analysis: (a) electron diffraction pattern of the second phase $Mg_2Ca$ (b,c) second phase.

**Figure 3.** (a,b) Surface potential map and potential profile of $Mg_2Ga$ phase, (c,d) surface potential map and potential profile of inclusion (Mg-Si-Ca-Fe), (e,f) surface potential map and potential profile of inclusion (Mg-Si-Ca), (g) SEM micrographs of Mg-Ca alloy with identified inclusions.

**Figure 4.** SEM surface morphologies: (a) PEO1-F, (b) PEO2-F and (c) PEO3 coatings.

**Figure 5.** BSE cross sections of the coatings: (a,b) PEO1-F, (c,d) PEO2-F and (e,f) PEO3 coatings.

**Figure 6.** X-Ray difractograms of the as-received coatings.

**Figure7.** (a-c) Live-dead staining and (d-f) SEM micrographs of the cell attachment after 3 d: (a,d) bare material, (b,e) PEO3 and (c,f) PEO1-F.

**Figure 8.** Potentiodynamic curves of substrate Mg-Ca, PEO1-F and PEO2-F.

**Figure 9.** Nyquist (a, d, g) and Bode (b, c, e, f, h, i) plots of the EIS spectra of (a-c) substrate Mg-Ca, (d-f) PEO1-F and (g-i) PEO2-F.

**Figure 10.** Equivalent circuits used to fit the EIS data for the substrate (a) and PEO coating after (b)1 h, (c) 3 and 7 d and (d) 28 d of immersion in SBF solution at 37 ºC.

**Figure 11.** Evolution of the resistance for (a) PEO1-F and (b) PEO2-F.

**Figure 12.** (a) Hydrogen evolution volume and (b) Hydrogen evolution rate for substrate and PEO coatings containing fluorides (c) Digital images after 10 weeks of immersion in SBF at 37 °C.

**Figure 13.** Cross-sections after immersion (a)substrate 4 w (b) substrate 8 w, (c) PEO1-F 4w, (d) PEO1-8w (e) PEO2-F 4w, (f) PEO2-8w.

**Figure 14.** Fluoride ions released for PEO coatings containing fluorides.

**Table**

**Table 1.** Parameters of the different PEO treatments

| **Coating** | **Electrolyte (g/L)** | **Time (s)** |
|---|---|---|
| **PEO1-F** | 10 g/L $Na_3PO_4$<br>1 g/L KOH<br>2.9 g/L CaO<br>8 g/L NaF | 420 |
| **PEO2-F** | 10 g/L $Na_3PO_4$<br>1 g/L KOH<br>2.9 g/L CaO<br>8 g/L NaF | 540 |
| **PEO3** | 10 g/L $Na_3PO_4$<br>1 g/L KOH<br>2.9 g/L CaO | 600 |

**Table 2.** EDS point analysis of Figure 3 g.

| | Mg | Al | Ca | Si | Mn | Fe |
|---|---|---|---|---|---|---|
| **Point 1** | 79.79 | 1.22 | 6.42 | 7.9 | 0.18 | 4.48 |
| **Point 2** | 82.69 | - | 7.24 | 10.07 | - | - |

**Table 3**. EDS point analysis of the coatings

| | | **Elements at. %** | | | | | | | |
|---|---|---|---|---|---|---|---|---|---|
| | Area | F | Na | Mg | P | K | Ca | O | Ca/P ratio |
| **PEO1-F** | outer | 15.53 | 5.65 | 18.67 | 5.97 | 0.11 | 8.80 | 45.27 | 1.47 |
| | intermediate | 24.97 | 4.19 | 30.71 | 1.97 | 0.14 | 0.11 | 37,91 | 0.05 |
| | inner | 27.10 | 1.51 | 32.39 | 1.67 | - | - | 37.33 | - |
| | Plan view | 11.2 | 2.8 | 30.22 | 3.13 | 0.15 | 4.52 | 47.68 | 1.44 |
| **PEO2-F** | outer | 13.25 | 0.91 | 20.61 | 6.84 | - | 10.12 | 48.28 | 1.48 |
| | intermediate | 16.92 | 1.11 | 30.82 | 3.71 | - | 3.39 | 44.05 | 0.91 |
| | inner | 25.94 | 3.23 | 31.19 | 1.62 | 0.20 | 0.43 | 37.39 | 0.26 |
| | Plan view | 22.9 | 2.4 | 16.9 | 5.2 | 0.1 | 10.5 | 41.9 | 2 |
| **PEO3** | outer | - | - | 46.06 | 0.95 | 0.08 | 0.015 | 52.76 | 0.16 |
| | inner | - | - | 47.06 | 1.50 | - | 0.06 | 51.38 | 0.04 |
| | Plan view | - | 0.37 | 46.84 | 1.25 | 0.08 | 0.63 | 50.83 | 0.5 |

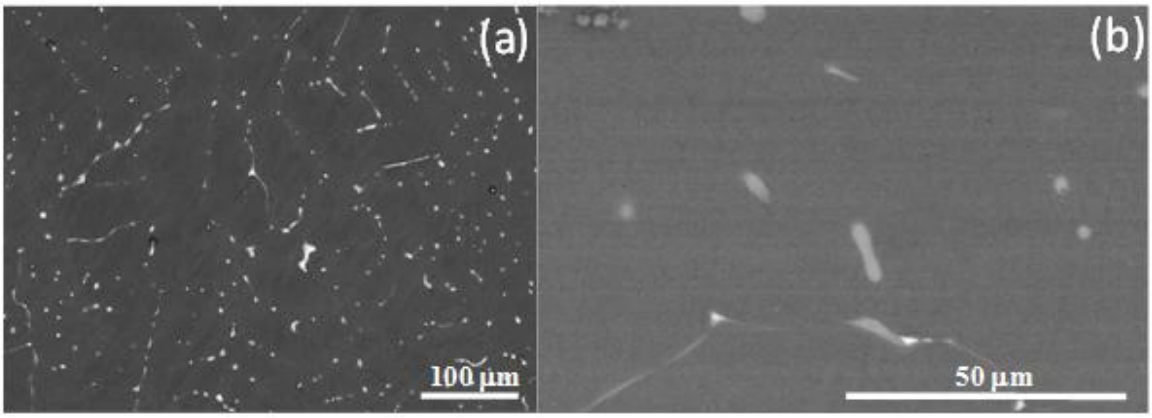

**Fig.1.** SEM micrographs of Mg-Ca alloy in as cast condition

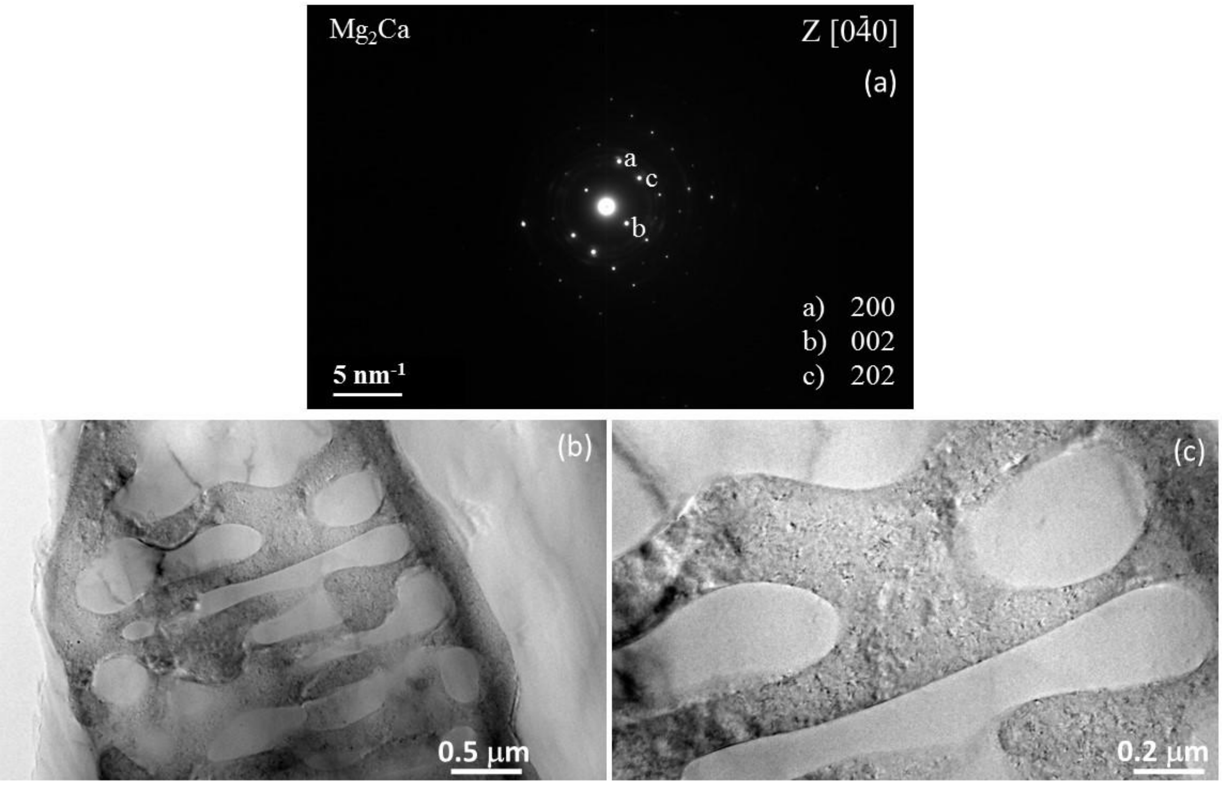

**Fig.2.** TEM analysis: (a) electron diffraction pattern of the second phase $Mg_2Ca$ (b,c) second phase

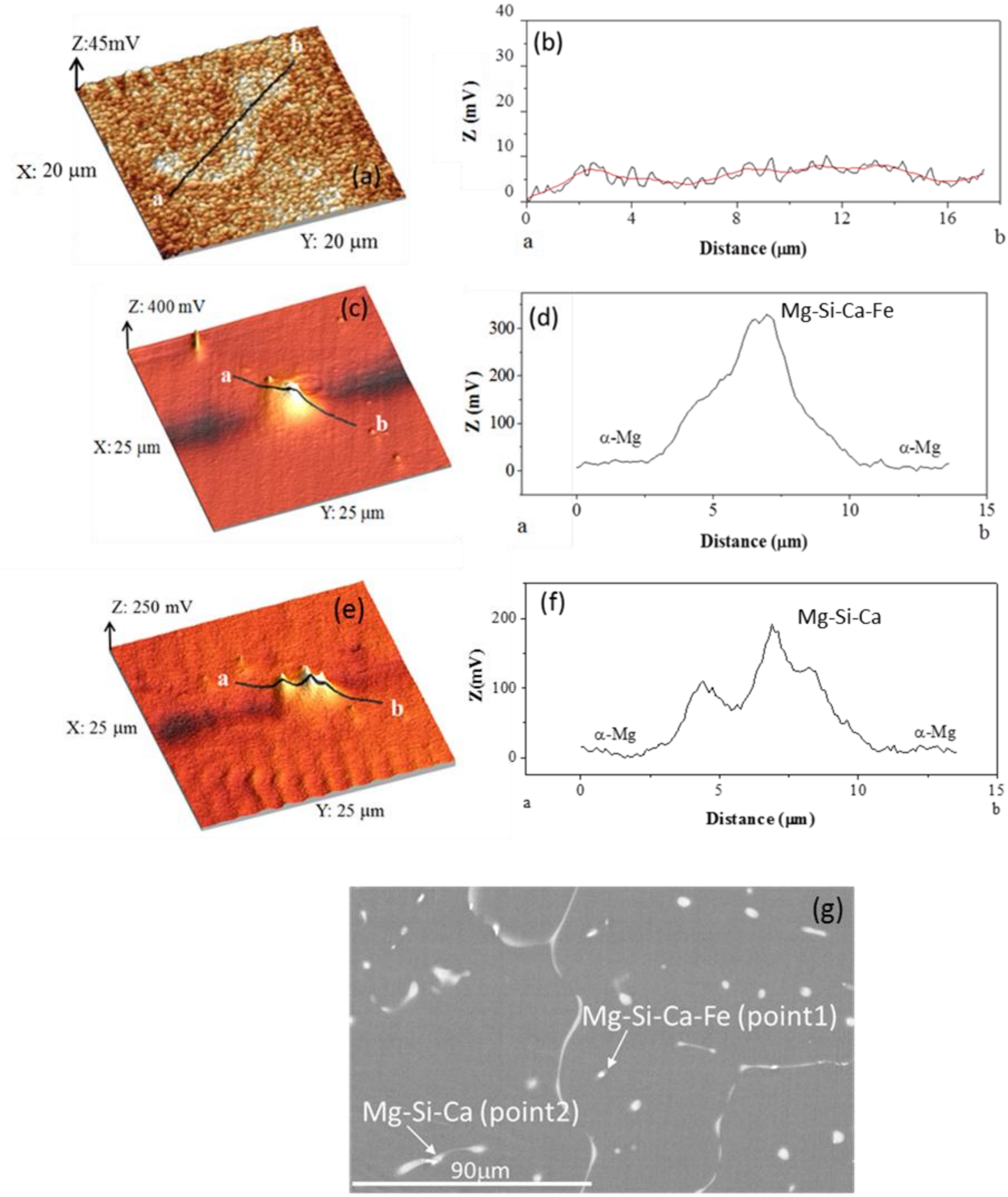

**Fig.3.** (a,b) Surface potential map and potential profile of $Mg_2Ga$ phase; (c,d) surface potential map and potential profile of inclusion (Mg-Si-Ca-Fe); (e,f) surface potential map and potential profile of inclusion (Mg-Si-Ca); (g) SEM micrographs of Mg-Ca alloy with identified inclusions

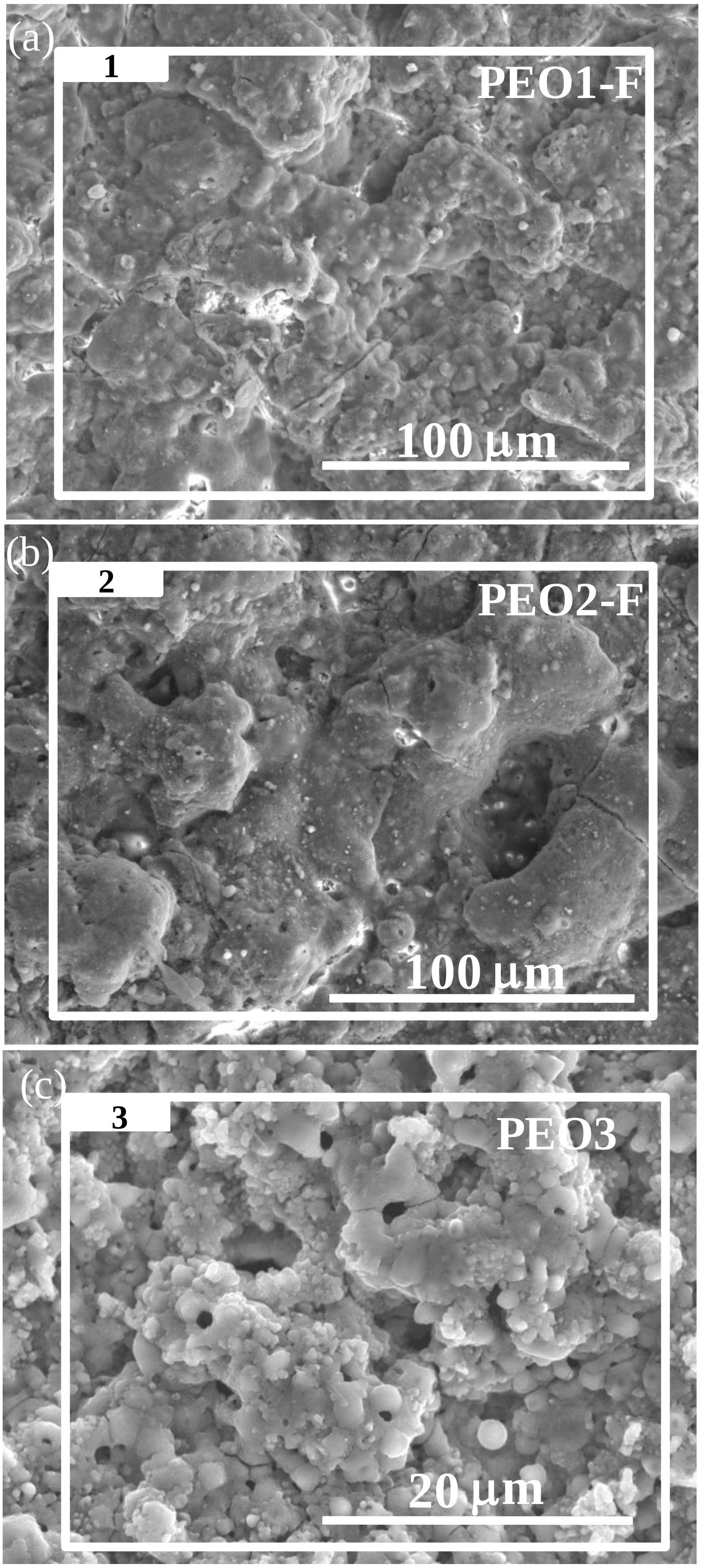

**Fig.4.** SEM surface morphologies: (a) PEO1-F, (b) PEO2-F and (c) PEO3 coatings

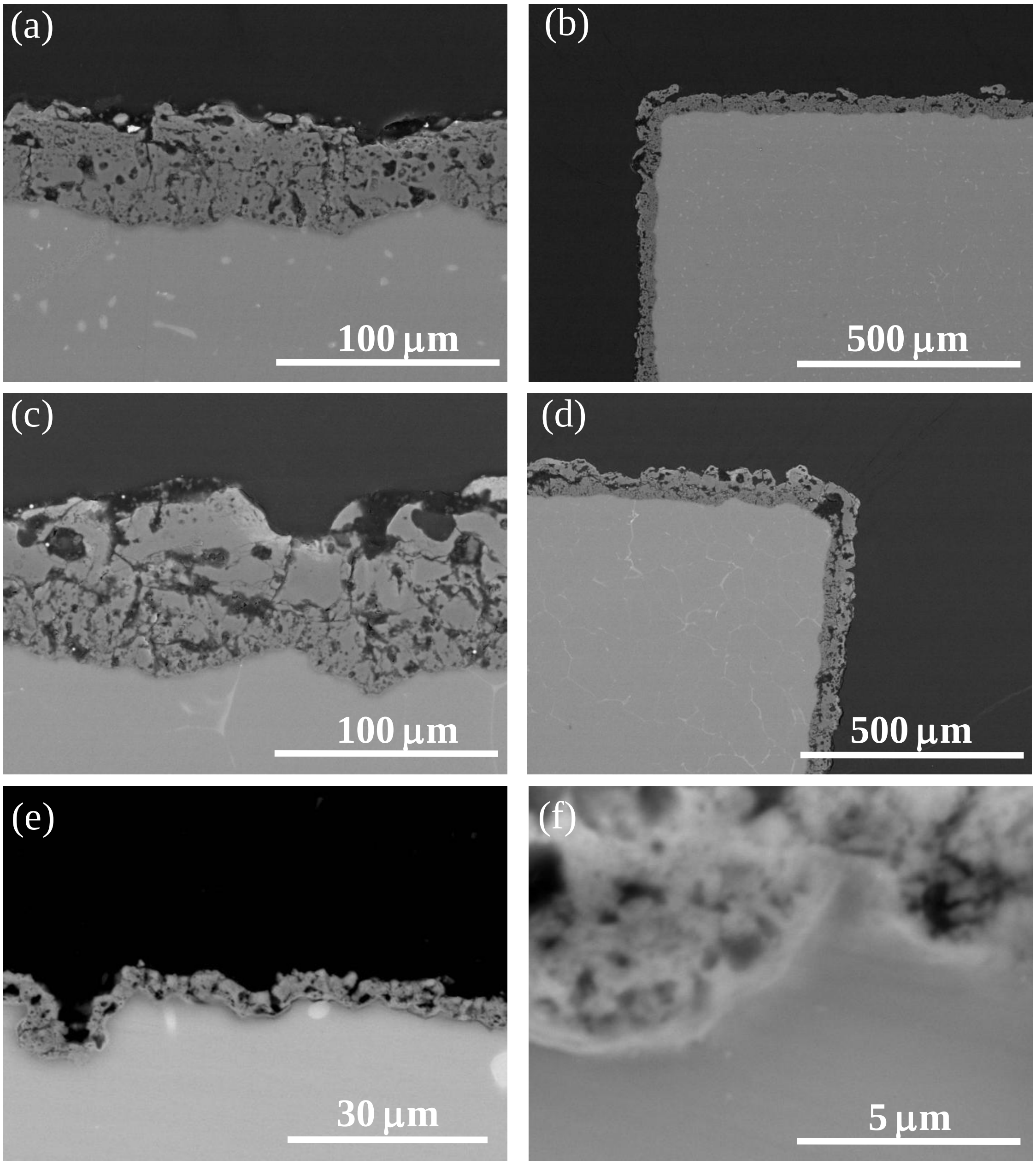

**Fig.5.** BSE cross sections of the coatings: (a,b) PEO1-F, (c,d) PEO2-F and (e,f) PEO3 coatings

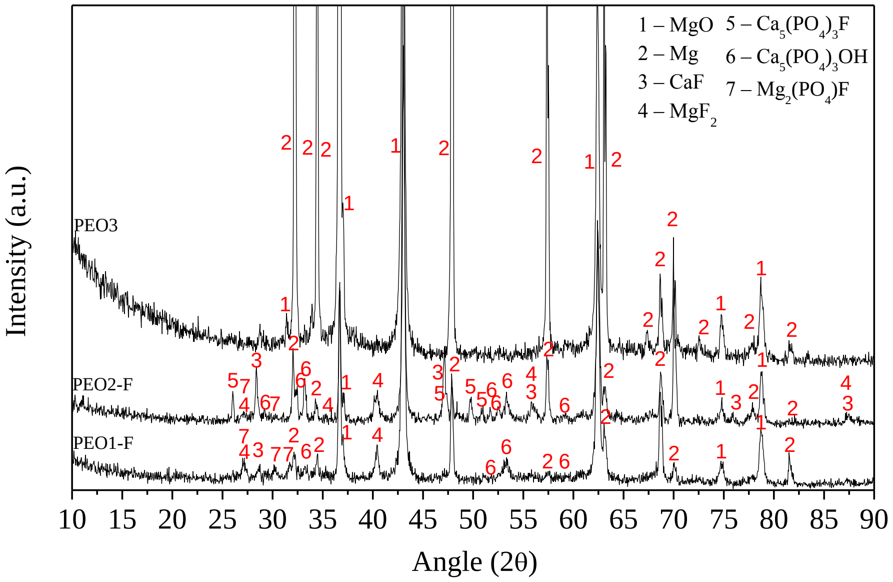

**Fig. 6.** X-Ray difractograms of the as-received coatings

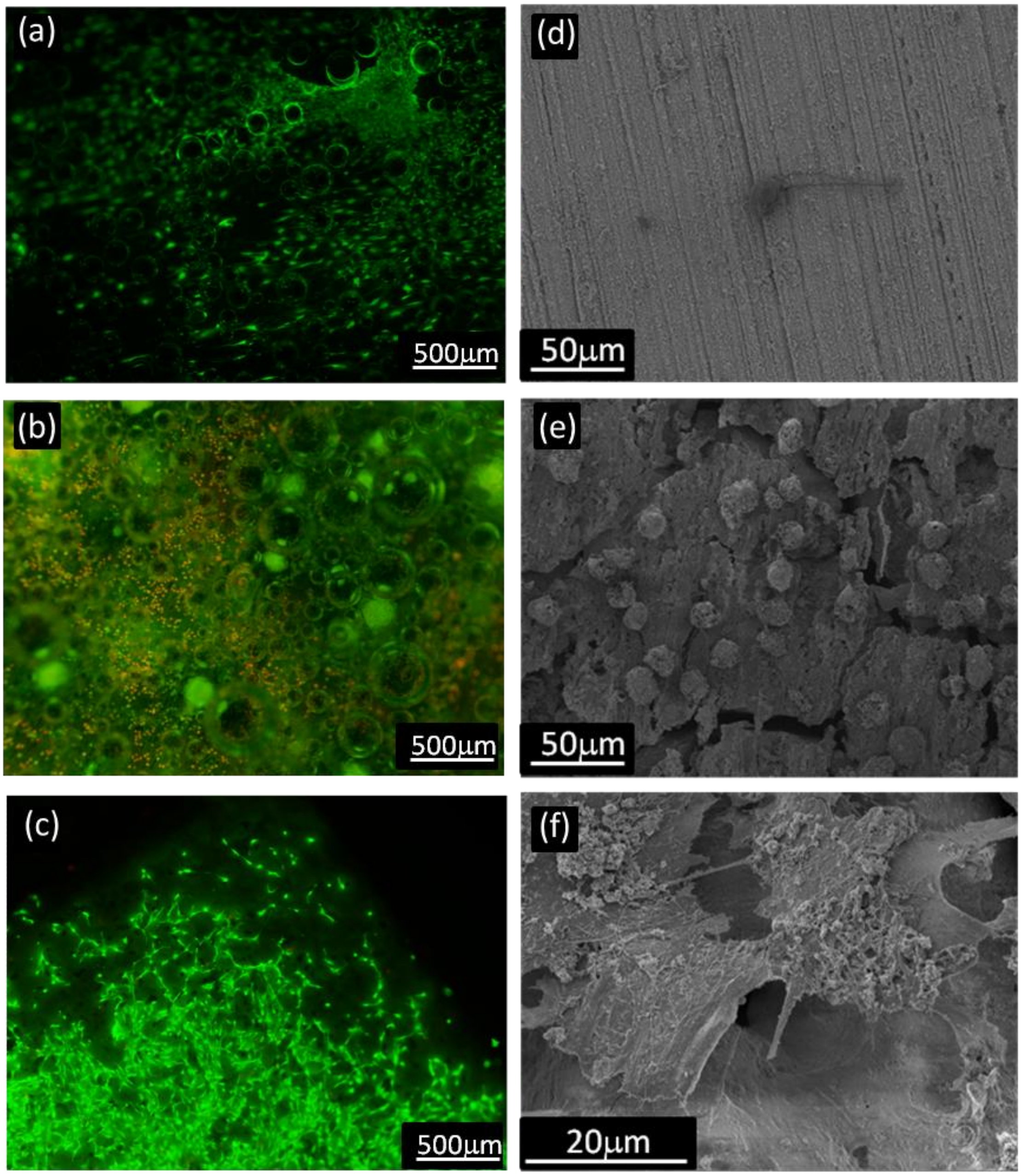

**Fig.7.** (a-c) Live-dead staining and (d-f) SEM micrographs of the cell attachment after 3 d: (a,d) bare material, (b,e) PEO3 and (c,f) PEO1-F

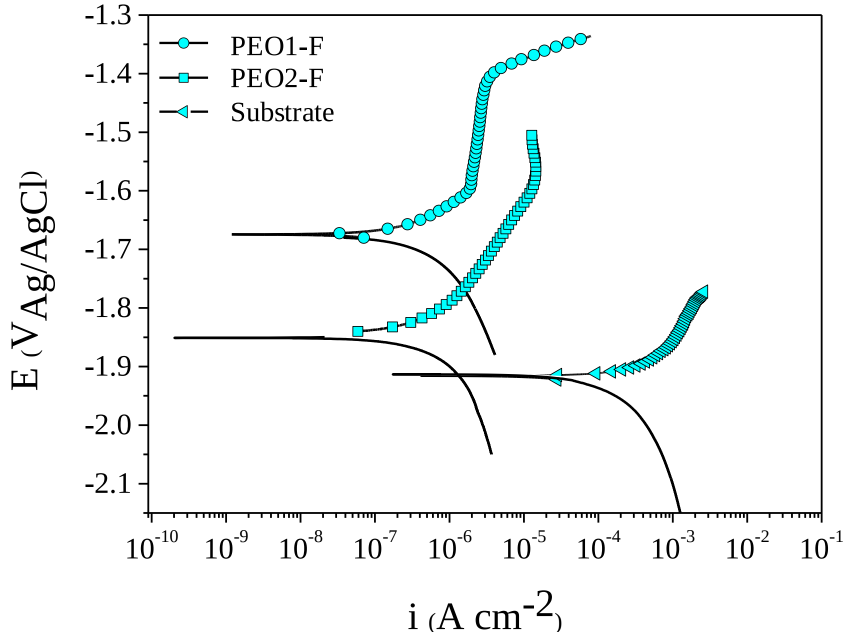

**Fig. 8.** Potentiodynamic curves of substrate Mg-Ca, PEO1-F and PEO2-F.

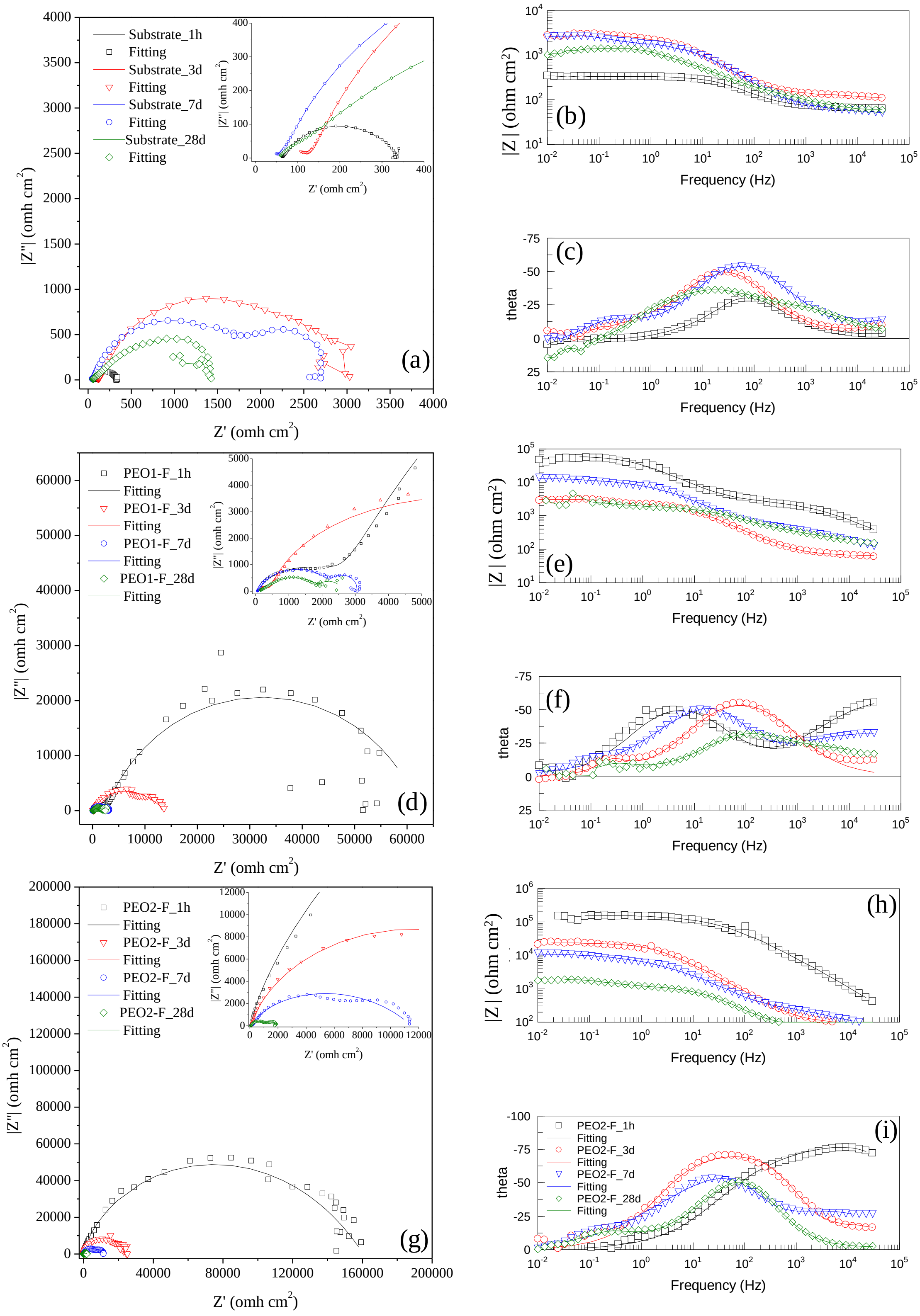

**Fig. 9.** Nyquist (a, d, g) and Bode (b, c, e, f, h, i) plots of the EIS spectra of (a-c) substrate Mg-Ca, (d-f) PEO1-F and (g-i) PEO2-F.

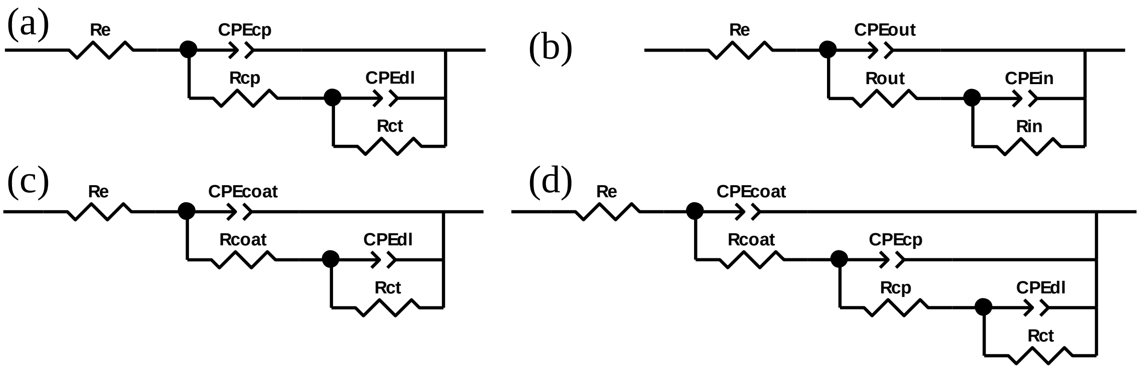

**Fig. 10.** Equivalent circuits used to fit the EIS data for the substrate (a) and PEO coating after (b) 1 h, (c) 3 d and 7 d and (d) 28 d of immersion in SBF solution at 37 ºC.

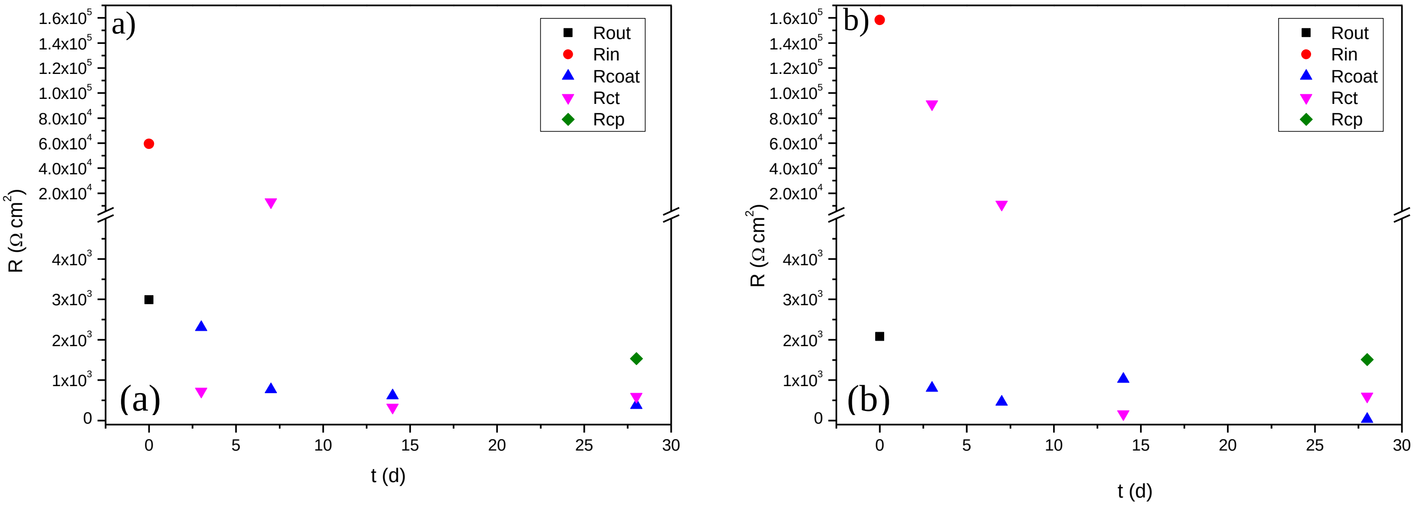

**Fig11.** Evolution of the resistance for (a) PEO1-F and (b) PEO2-F

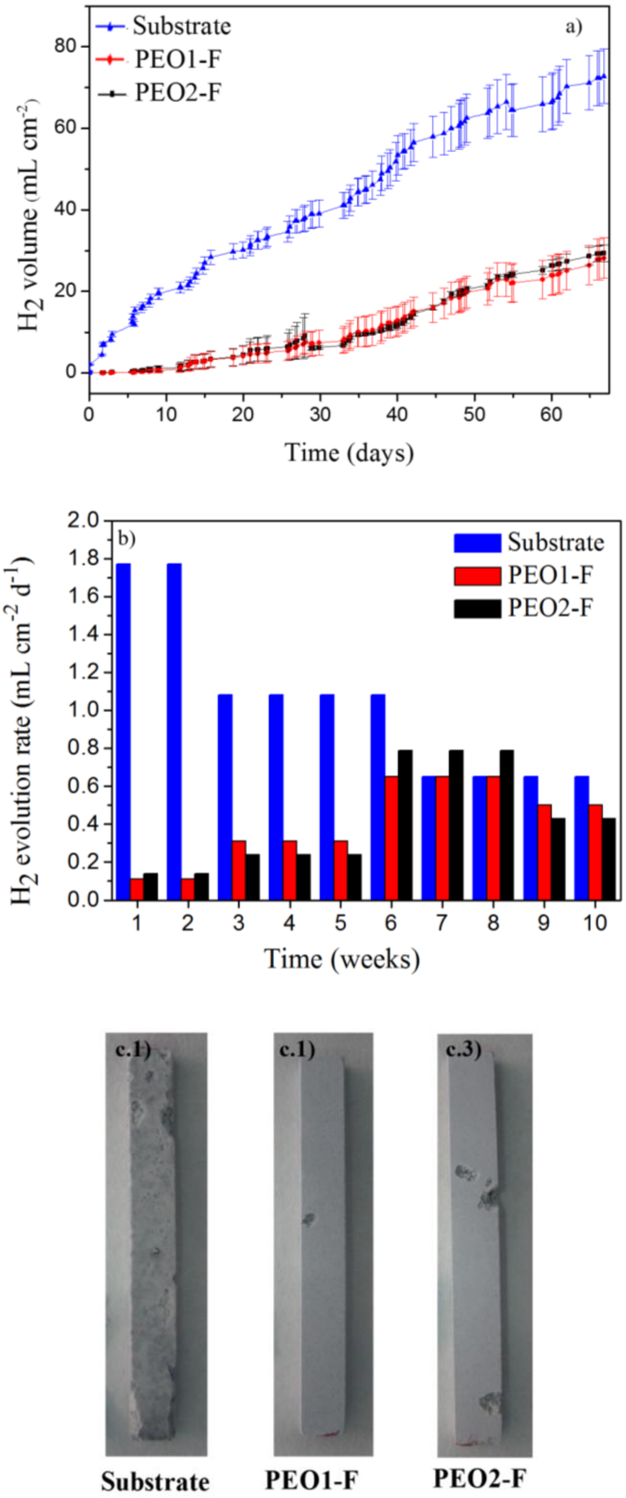

**Fig. 12.** (a) Hydrogen evolution volume and (b) Hydrogen evolution rate versus time for substrate and PEO coatings containing fluorides (c) Digital images after 10 weeks of immersion in SBF.

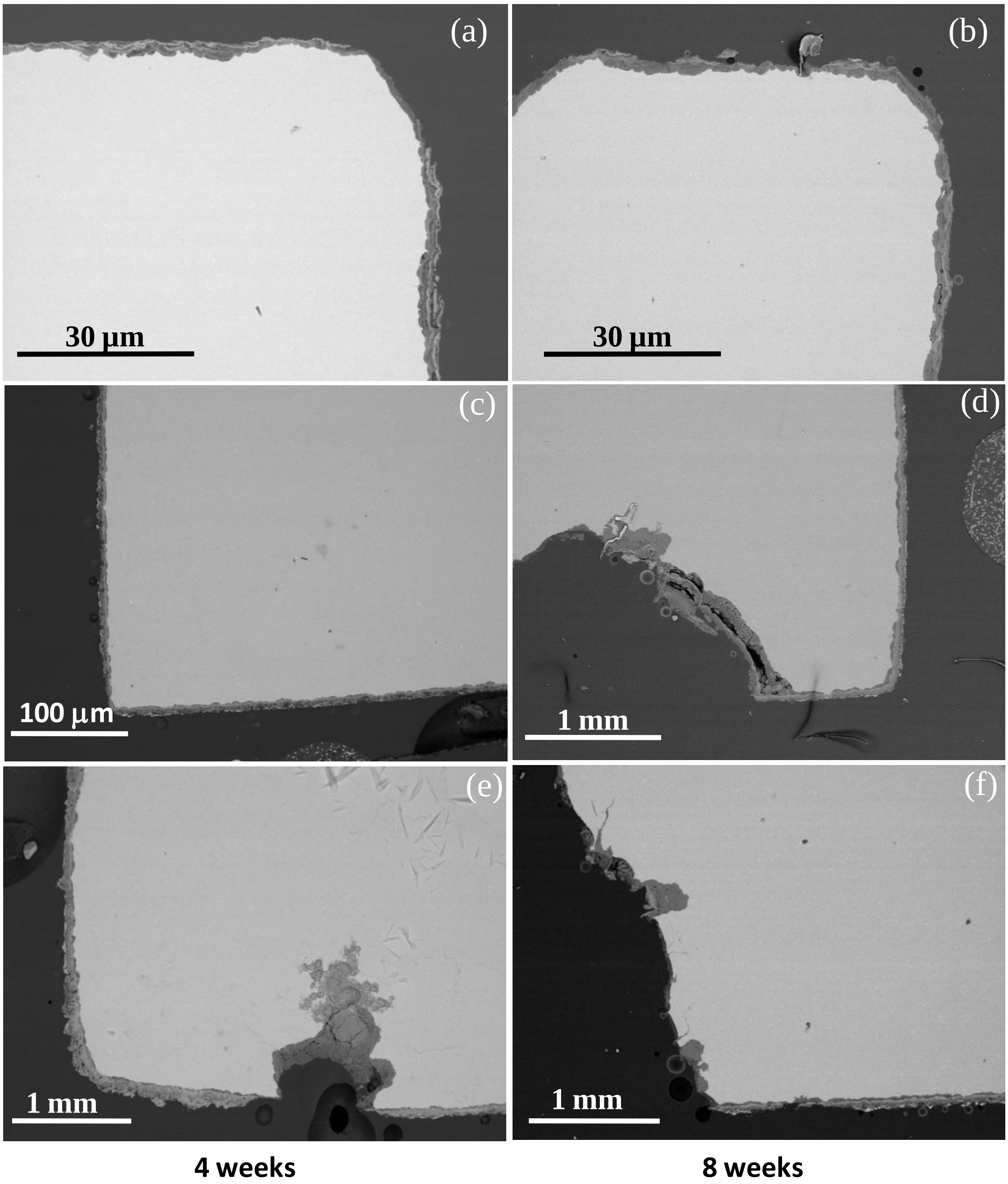

**Fig. 13.** Cross-sections after immersion (a) substrate 4 w, (b) substrate 8 w, (c) PEO1-F 4 w, (d) PEO1-F 8 w (e) PEO2-F 4w, (f) PEO2-F 8 w.

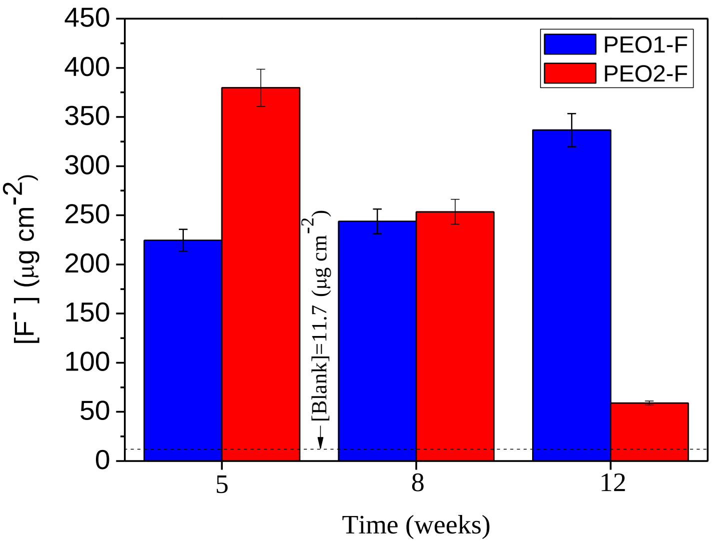

**Fig. 14.** Fluoride ions released for PEO coatings containing fluorides

Suggested Reviewers

1.Sannakaisa Virtanen

Chair for Surface Science and Corrosion, Department Materials Science

University of Erlangen-Nuremberg,Germany

virtanen@ww.uni-erlangen.de

Field of expertise: Surface modification and degradation of Mg based materials

2. Sungmo Moon

Korea Institute of Materials Science

Republic of Korea

sungmo@kims.re.kr

Field of expertise: Plasma electrolytic oxidation coatings. Corrosión of light alloys

3. Belen Torres

Dpto. de Ciencia e Ingeniería de Materiales

Universidad Rey Juan Carlos, Spain

belen.torres@urjc.es

Field of expertise: Surface modification of magnesoium based materials. Corrosion of light alloys

**Graphical Abstract (for review)**

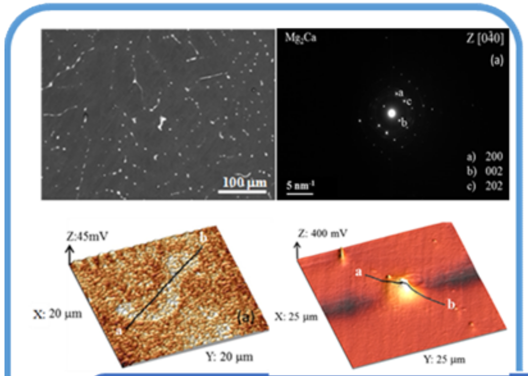

Biodegradable Mg alloys design: Mg-Ca alloy

Degradation control: Bioactive PEO coatings

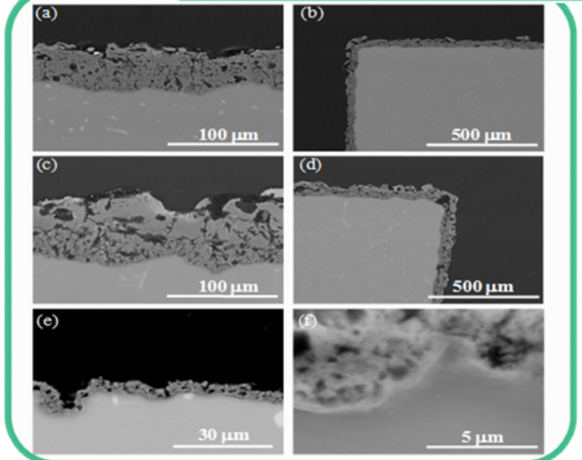

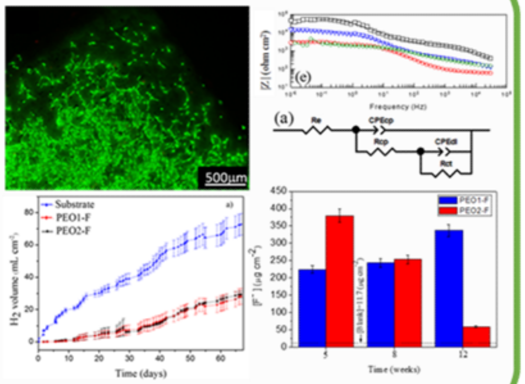

*Biological investigation

*Corrosion behaviour

*Fluoride release